scientific reports

Check for updates

OPEN

Effective Landé factors for an electrostatically defined quantum point contact in silicene

Bartłomiej Rzeszotarski[1]✉, Alina Mreńca-Kolasińska[1,2], François M. Peeters[3] & Bartłomiej Szafran[1]

The transconductance and effective Landé g^* factors for a quantum point contact defined in silicene by the electric field of a split gate is investigated. The strong spin–orbit coupling in buckled silicene reduces the g^* factor for in-plane magnetic field from the nominal value 2 to around 1.2 for the first- to 0.45 for the third conduction subband. However, for perpendicular magnetic field we observe an enhancement of g^* factors for the first subband to 5.8 in nanoribbon with zigzag and to 2.5 with armchair edge. The main contribution to the Zeeman splitting comes from the intrinsic spin–orbit coupling defined by the Kane–Mele form of interaction.

Quantum point contacts (QPC) in spin–orbit-coupled semiconductors are elementary elements in the construction of spin-active devices due to their ability to enhance the effective Lande factor g^*[1]. In the absence of external magnetic field QPC system with strong spin–orbit interaction (SOI) can work as a spin filter[2–6]. Spin orbit interactions due to the crystal lattice asymmetry and external electric fields introduce effective magnetic fields[7–9] for the flowing electrons. The orientation of an external magnetic field (in-plane or out-of-plane) has a strong impact on conductance due to the spin spatial anisotropy of the spin–orbit field[10–12] which has been observed experimentally[13,14] by splitting the transconductance lines. In systems with strong SOI the anisotropy is very strong, e.g. in InSb QPCs[15] the in-plane $|g^*| = 26$ and out-of-plane is two times higher, $|g^*| = 52$ for the lowest conducting subband. In black phosphorus thin films in which quantum Hall effect has been observed[16] the $g^* \approx 2$ for the in-plane magnetic field and approaches 2.0 with increasing hole doping density for perpendicular orientation[17]. On the other hand, in materials with low intrinsic spin–orbit coupling such as pristine graphene, the g^* value is $\simeq 2$ as for free electrons[18–20]. In bilayer graphene (BLG) structures quantum point contacts can be formed electrostatically[21–25] due to the opening of a band gap that can be tuned by a perpendicular electric field[26–30]. The spin g^* is still $\simeq 2$ in bilayer graphene QPC[24], however the valley g factor can be tuned and used as an additional degree of freedom. In the silicene[31–34], a graphene-like honeycomb structure, two sublattices displaced in z direction introduce strong intrinsic spin orbit interaction[35]. Additionally, the band gap in silicene can be electrostatically modified by external gates[36–39] that makes it a good candidate for a spin-active device.

In this paper we present a numerical calculation of the effective Landé g^* factors for silicene using the transconductance lines according to a standard experimental procedure of determining the g^* values[13,14,40–42]. We expect that silicene stabilized on non-metallic substrate used in future experiments will behave in the same manner as pristine silicene which Hamiltonian we use in our calculations, for instance: (1) Al_2O_3[43] induces band gap in K point along with minigaps in the band structure in silicene, or (2) InSe[44] that effectively introduce electrical potential to the silicene. Nevertheless, both substrates preserving Dirac-like electronic characteristics in silicene.

We test the g^* anisotropy by dependence on the orientation of the external magnetic field. We discuss the impact of the SO interaction on g^* value for in-plane and out-of-plane magnetic field. We simulate experimental path (transconductance method) of g^* measurements to give exact explanation what uncertainities can occur during the analysis of the experimental data, we present full description from the theoretical calculations on how to interpret the armchair valley/subbands in the transconductance map, and also how to explain differences of armchair/zigzag transconductance in terms of SOI impact (the spin–orbit interaction produces different shifts to the subbands for zigzag/armchair ribbon in different way considering perpendicular magnetic field). Those explanations hold not only for silicene, but all 2D-Xenes (germanene, stanene) or other 2D materials with strong SOI in Kane–Mele form. The novelty of this work over the previous one[42] relies on the Hamiltonian which

[1]Faculty of Physics and Applied Computer Science, AGH University of Science and Technology, al. Mickiewicza 30, 30-059 Kraków, Poland. [2]Department of Physics, National Cheng Kung University, Tainan 70101, Taiwan. [3]Departement Fysica, Universiteit Antwerpen, Groenenborgerlaan 171, 2020 Antwerp, Belgium. ✉email: rzeszotarski@fis.agh.edu.pl

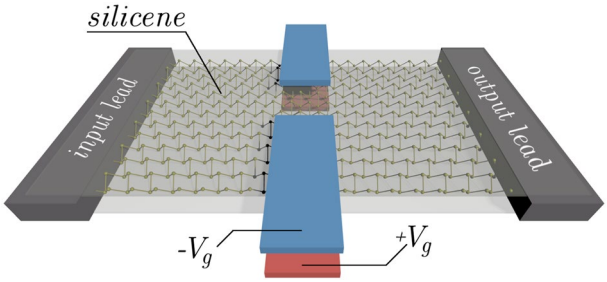

Figure 1. Schematic view of the system. A silicene nanoribbon is sandwiched between dielectric layers. Two pairs of external gates provides electric potential V_g equalizing the effective energy on both sublattices.

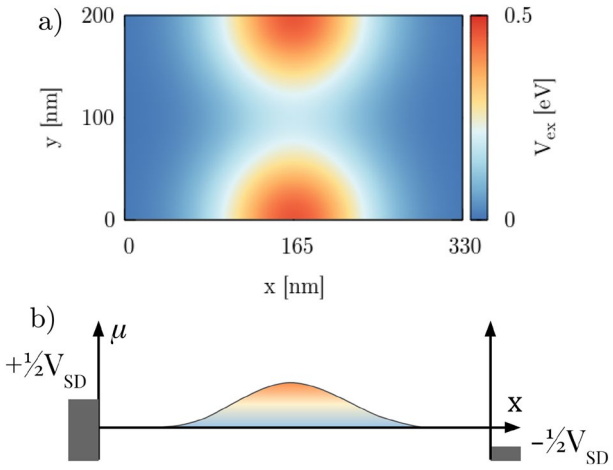

Figure 2. (**a**) Map of the external electric potential for $V_g = 0.5$ eV, in the system of size 200 nm by 330 nm. Two Gaussian 2D potentials are used to form the quantum point contact in the middle of the silicene nanoribbon. (**b**) Profile of the QPC. The occupied states below chemical potential ($\pm V_{SD}/2$) are marked on both sides by rectangles with the assumption of a symmetric drop along the device.

contains the Kane–Mele form of SOI in tight-binding Hamiltonian of pristine silicene. There were no previous studies on silicene that describe g^* measurement in this manner.

Theory

We consider a device with a quantum point contact defined in silicene nanoribbon (Fig. 1). The QPC profile is defined by external split gates at voltages $\pm V_g/(-e)$ which induce a potential V_{ex} at both sublattices equally forming QPC profile. In our calculations, we assume a model potential profile given by a Gaussian[45]

$$V_{Gauss}(x, y; x_0, y_0, \Delta x, \Delta y) = V_g e^{\frac{-(x-x_0)^2}{(2\Delta x)^2}} e^{\frac{-(y-y_0)^2}{(2\Delta y)^2}} \tag{1}$$

and model the QPC with

$$V_{ex} = V_{Gauss}(x, y; 165\,\text{nm}, 0\,\text{nm}, 40\,\text{nm}, 40\,\text{nm}) + V_{Gauss}(x, y; 165\,\text{nm}, 200\,\text{nm}, 40\,\text{nm}, 40\,\text{nm}). \tag{2}$$

The higher the applied gate voltage, the narrower the conductive channel in the center of the QPC. Figure 2 presents an example of gate energy distribution within silicene for the specific case where $V_g = 0.5$ eV (Fig. 2a), and the profile of the potential (Fig. 2b).

Hamiltonian. We use the low-energy effective Hamiltonian with spin–orbit coupling for silicene, that is derived by Liu et al.[46] from symmetry considerations and the tight-binding method combined with first-principles calculations. This Hamiltonian is very general because it applies also to the graphene (when planar geometry of the structure is considered) as well as for graphene low-buckled counterparts like germanene and stanene. We use it in the form:

$$H_{eff} = -t \sum_{\langle k,j\rangle,\chi} c^\dagger_{k\chi} c_{j\chi} + e\mathbb{E}_z \sum_{k,\chi} \gamma_k c^\dagger_{k,\chi} c_{k,\chi}, + \frac{1}{2} g\mu_B \sum_{k,\chi,\varrho} c^\dagger_{k,\chi} c_{k,\varrho} (\mathbf{B}\cdot\boldsymbol{\sigma})_{\chi\varrho} + H_{SO}, \tag{3}$$

where we use creation ($c^{\dagger}_{k\chi}$) and annihilation ($c_{k\chi}$) operators for an electron on site k with spin χ. Ions in the nearest neighborhood are specified by $\langle k,j\rangle$. $t = 1.6$ eV is the hopping parameter[35,46] and e is the elementary electric charge. The $\mathbb{E}_z$ term describes the external perpendicular electric field with a factor $\gamma_k = \frac{1}{2}\cdot 0.46$ Å that determines the offset in the sublattices. The penultimate term introduces the external magnetic field $\mathbf{B} = [b_x, b_y, b_z]$ to the system, where $\boldsymbol{\sigma} = [\sigma_x, \sigma_y, \sigma_z]$ is a vector of Pauli matrices. We use the Landé factor $g = 2$ for electrons in silicene along with the Bohr magneton μ_B. The last term describes the spin–orbit part of the effective Hamiltonian H_{eff}:

$$H_{SO} = t_{KM}\sum_{\langle\langle k,j\rangle\rangle\chi,\varrho}\nu_{kj}c^{\dagger}_{k\chi}\sigma^{z}_{\chi,\varrho}c_{j\varrho} + t_R\sum_{\langle\langle k,j\rangle\rangle\chi,\varrho}\mu_{kj}c^{\dagger}_{k\chi}\left(\boldsymbol{\sigma}\times\boldsymbol{d}_{kj}\right)^{z}_{\chi\varrho}c_{j\varrho}, \tag{4}$$

where the first part describes the intrinsic spin–orbit coupling in Kane–Mele (KM) form[8,47] with $t_{KM} = i\frac{\lambda_{SO}}{3\sqrt{3}}$ and $\lambda_{SO} = 3.9$ meV, while the second term is an intrinsic Rashba SOI $t_R = -i\frac{2}{3}\lambda_R$ with $\lambda_R = 0.7$ meV[35,46]. The summation in both cases runs over next-nearest neighbor ions $\langle\langle k,j\rangle\rangle$, where μ_{kj} is +1 or −1 for sublattice A and B, respectively. The $\nu_{kj} = +1\,(-1)$ for the counterclockwise (clockwise) hopping from j to k ion, where $\boldsymbol{d}_{kj}$ is a vector pointing from ion k to ion j. The lattice constant $a = 3.86$ Å. To calculate the total conductance we use the Landauer formalism

$$G = \frac{e^2}{\hbar}T_{total}(E_F) = \frac{e^2}{\hbar}\sum_{m}^{N}T_m, \tag{5}$$

where N is the total number of propagating modes and T_m is the transmission probability of the mth mode from the input to the output lead. We use quantum transmitting boundary method to solve the scattering problem[42]. For finite potentials of source and drain the current is calculated as follows:

$$I(V_{SD};\,T=0) = \frac{e}{h}\int_{-e\frac{V_{SD}}{2}}^{+e\frac{V_{SD}}{2}}T_{total}(E_F+E)dE, \tag{6}$$

with the assumption of a drop of the potential along the device for nonequivalent chemical potential of the leads (Fig. 2b). With a nonzero bias, we use the formula for the conductance

$$G = \frac{dI(V_{SD})}{dV_{SD}} \tag{7}$$

and we define the transconductance dG/dV_g as a second mixed derivative of the current,

$$\frac{dG}{dV_g} = \frac{d^2I(V_{SD})}{dV_{SD}dV_g}. \tag{8}$$

The classical procedure of calculating the effective Landé g* factors from transconductance is based on compensation of the Zeeman splitting by application of source-drain bias into the system along with energy modulation from the gate potential[13,14,40,41]. The gate-to-energy conversion factor can be determined for each subband from the slope of the transconductance lines in $B = 0$ according to the formula:

$$\xi_m = \frac{1}{2}\frac{dV_{SD}}{dV_g} \tag{9}$$

where the 1/2 factor results of source-drain potential shift that is equal to half of the applied bias: $1/2\,V_{SD}$. The final step in the procedure of finding g^* factors is to evaluate the transconductance as a function of magnetic field B, and for each subband to find the susceptibility as the derivative $\frac{d(\Delta V_g(B))}{dB}$. Then the effective Landé factor for mth subband is given by

$$g^*_m = \frac{1}{\mu_B}\frac{d(\Delta V_g(B))}{dB}\xi_m. \tag{10}$$

Results

To reduce the numerical cost of the calculations we use the scaling method[32] with a scaling factor $s_f = 4$, that gives new crystal lattice constant $a_s = a\cdot s_f$ along with new hopping parameter $t_s = \frac{t}{s_f}$. We replace a to a_s and t to t_s in Hamiltonian (4). All the results below are presented for the Fermi energy $E_F = 0.07$ eV, if not stated otherwise.

Band structure. For the constriction center of the QPC we calculate the band structure for two different edge types: armchair and zigzag. In the zigzag case with NO SOI ($H_{SO} = 0$) we observe spin-degenerate subbands at $\mathbf{B} = 0$ (Fig. 3a) for both valleys K' and K, while this degeneracy is lifted upon applying an external magnetic field perpendicular to the sample (Fig. 3c for $B_z = 2$ T) that slightly splits the spin-states and shifts the subbands higher for K and lower for K'. When all spin–orbital interactions are included ($H_{SO} \neq 0$) then degeneracy is lifted even at $\mathbf{B} = 0$, since the Zeeman-like SO interaction in KM interaction[8,47] introduces an

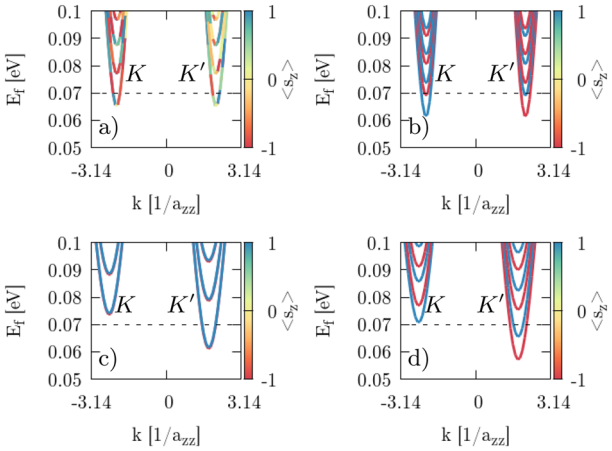

Figure 3. Band structure of silicene nanoribbon with zigzag edges calculated for the center of the QPC constriction with $V_g = 0.15$ eV, with NO SOI (**a**, **c**) and with SOI (**b**, **d**). Magnetic field is equal to $B_z = 0$ (**a**, **b**) and $B_z = 2$ T (**c**, **d**). The black dashed line denotes the Fermi energy $E_F = 0.07$ eV. The color bar indicates the mean value of the spin projection along z axis. The $a_{zz} = 3a_s$ is the zigzag lattice constant.

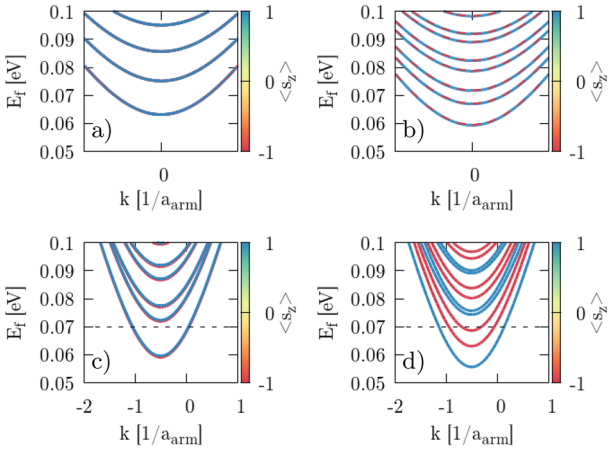

Figure 4. Same as Fig. 3 but for a nanoribbon with armchair edges. Armchair lattice period is equal to $a_{arm} = \frac{6a_s}{\sqrt{3}}$.

effective magnetic field with an amplitude along the z axis that splits the spin-states in the subbands (Fig. 3b). Up (↑) spin states decrease their energy in the K valley and increase in the K' valley, while down (↓) spin states shift in an opposite way. Applying an external perpendicular magnetic field in the case with SOI taken into account changes the energy gap in the same manner as with NO SOI (Fig. 3d). We observe an analogous behavior for the armchair type of edges (Figs. 4, 5).

Conversion factors. We calculate the transconductance with a bias V_{SD} applied using Eqs. (6)–(8). Figure 6 presents maps of transconductance for armchair and zigzag edges for the cases – with spin–orbit interactions included or neglected in the Hamiltonian. The dependence of the energy shift in subbands introduced by the gate voltage V_G and compensated by source-drain bias V_{SD} are marked by straight dashed lines for each subband with NO SOI (Fig. 6c, d). For each subband we calculate the conversion factors (Eq. 9) from the slope of the corresponding line $\frac{dV_{SD}}{dV_g}$ for both types of nanoribbons: armchair and zigzag. Results are presented in Table 1.

In the case with SOI taken into consideration (Fig. 6a, b) we observe twice more subbands that emerge from splitting caused by the Zeeman-like part of the intrinsic SO coupling.

Effective Landé factors. We calculate the transconductance by taking the derivative of the G maps with respect to V_g. First we consider perpendicular magnetic field $B_\perp = \mathbf{B} = (0, 0, B_z)$. We present results for $H_{SO} = 0$ (Fig. 7) only for the zigzag nanoribbon since for the armchair system similar results are obtained. The two separate spin-states cannot be distinguished from the transconductance map so the calculation of the effective Landé factor is not possible in the standard way. However, we are able to identify valley and spin-state from

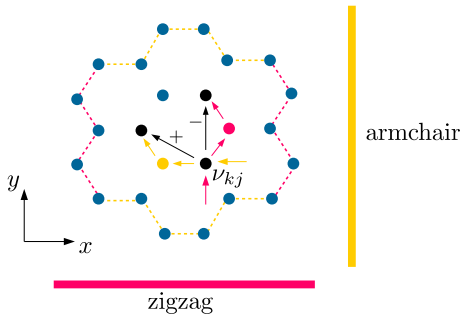

Figure 5. Schematic view of the ν_{kj} (Eq. 4) sign for two different edge types of silicene. For the same considered atom j paths to the next-nearest neighbor k differ in zigzag and armchair configuration and produce opposite sign of the local effective magnetic field resulting from KM term. This will produce mirrored image of spin signs in subband structures for armchair and zigzag.

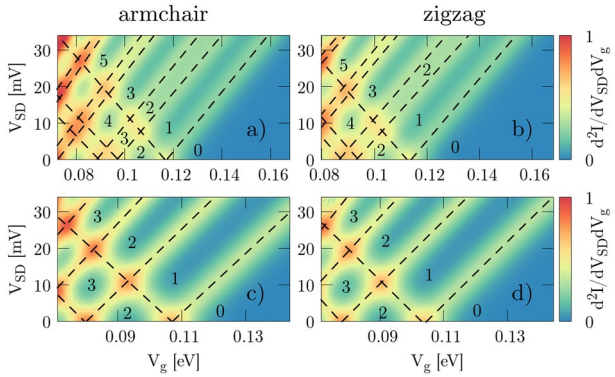

Figure 6. The transconductance $d^2I/dV_{SD}dV_g = \frac{dG}{dV_g}$ for armchair (**a**, **c**) and zigzag (**b**, **d**) nanoribbons with SOI (**a**, **b**) and NO SOI (**c**, **d**). Dashed lines denote the conductance levels (marked by numbers) and are used to calculate gate-voltage to energy conversion factors.

	ξ_1	ξ_2	ξ_3
Armchair	0.40	0.42	0.47
Zigzag	0.41	0.44	0.49

Table 1. Conversion factors for the first three subbands calculated from the transconductance (Fig. 6) with NO SOI.

the band structure in Fig. 7b. Upon subtraction of the energies at different B_z/V_g values we find $g^* = 2.0$, which agrees with the expected value $g = 2$ for electrons in silicene.

For nonzero H_{SO} in the Hamiltonian (3) the intrinsic SO interaction in the Zeeman-like form separates the spin states, and they can be easily distinguished in the transconductance map (Fig. 8) when external magnetic field B_z is applied. Identification of the subband and valley number in the armchair case comes from the band structure of the zigzag nanoribbon (Fig. 3) and can be explained as follows. Due to the symmetry of a silicene structure we can reduce the dimension of a system by cutting 2D infinite silicene sheet into ribbon with zigzag/armchair type of edge that is represented by single unit cell repeated infinitely along 1D. This reduction acts on the reciprocal lattice as well. The K/K' points are geometrically on atom position at A/B sublattice forming Dirac cones. 1D periodic boundary conditions allows us to calculate band structure for zigzag/armchair ribbons where dimension reduction does not move K/K'. Hence, we obtain 1D projection of the 2D band structure in reciprocal lattice picture where K/K' are distinguishable for zigzag edge. Armchair ribbon is made after rotation of $\frac{\pi}{2}$ with respect to zigzag, and in this projection K/K' are oriented along axis of unfolding periodic boundaries, resulting in full mixing of K/K' valley in the band structure. In this case we distinguish valley using zigzag band structure (Fig. 3) along with Fig. 5. Comparing information from those two figures with Fig. 4 we can deduce which exact spin subband is generated in K/K'. Calculating the slope of $d(\Delta V_g(B))/dB$ (marked by dashed lines) and using Eq. (10) with conversion factors (Table 1) we obtain $g_1^* = 5.8$, $g_2^* = 13.3$ for the case with zigzag edges and

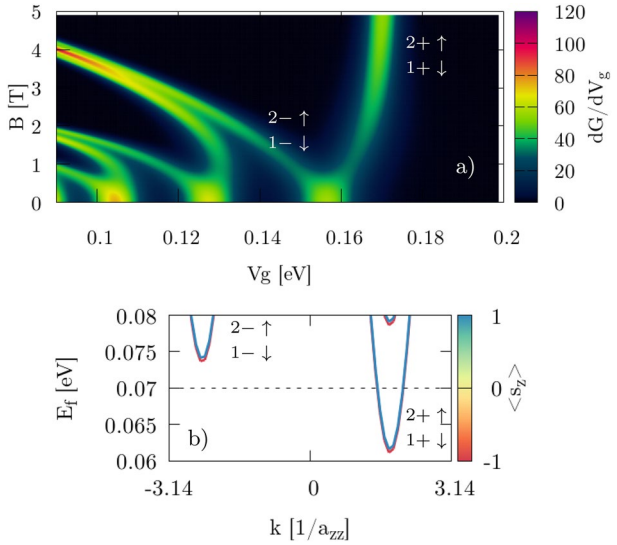

Figure 7. (**a**) Transconductance for the perpendicular $B\perp$ orientation of the magnetic field with NO SOI. Two first (1, 2) subbands are marked in K' (+) and K (−) valley with spin up (↑) and down (↓). Smooth transconductance peaks correspond to new conductive states in the paired spin-subbands which are close enough not to be seen as separate peak [see zoom in plot (**b**)]. Results are for zigzag edges.

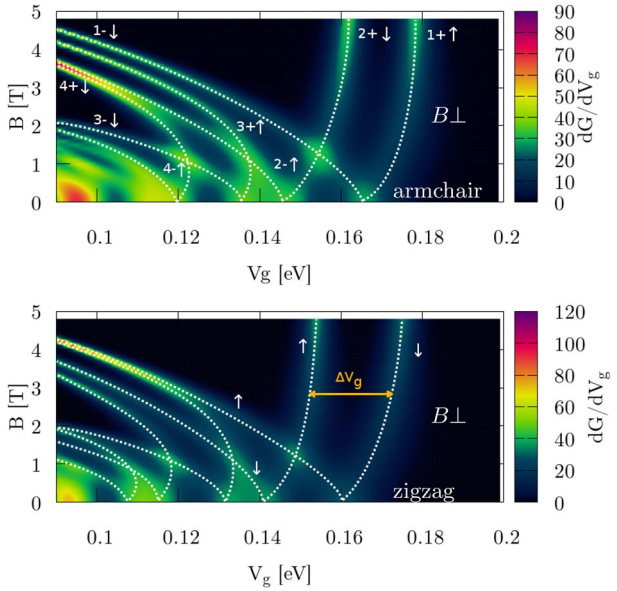

Figure 8. Transconductance for perpendicular $\mathbf{B} = [0, 0, B_z]$ orientation of external magnetic field applied to the system with active SO (nonzero terms in Hamiltonian). Numbers denote the subband index in K' valley (+) and K (−) with spin ↑ (↓) marked by white dotted lines. The ΔV_g term is calculated between two spin-correlated subbands within the same valley band.

$g_1^* = 2.5, g_2^* = 14.0$ for armchair edges (Table 2). The difference comes directly from the geometry (Fig. 5) where ν_{kj} in KM term defines the sign of an additional energy to spin states. Applying external magnetic field compensates this energy if its direction agrees with the emerged local magnetic field $\left[\frac{d(\Delta V_g(B))}{dB} > 0 \text{ for } K' \ (k > 0) \text{ in zigzag}\right]$, or forfeit for the opposite directions $\left[\frac{d(\Delta V_g(B))}{dB} < 0 \text{ for } K \ (k < 0) \text{ in zigzag}\right]$. We obtain mirrored behavior in armchair nanoribbons due to the ν_{kj} sign. In Fig. 10c, d we see that the slope for the first subband (N_1) is positive in the zigzag structure and negative in the armchair. Small difference in g_2^* (slopes N_2 in Fig. 10c, d) for armchair and zigzag comes from the fact that deeper conductive bands have higher energy and additional fraction that comes from KM term is less significant in this scenario.

SO off	g_1^*	g_2^*	g_3^*
$B_\parallel$	2.1	2.2	2.1
$B_\perp$	2.0	2.0	2.0
SO on	g_1^*	g_2^*	g_3^*
$B_{\parallel zz}$	1.2	0.78	0.45
$B_{\parallel a}$	1.17	0.92	0.32
$B_{\perp zz}$	5.8	13.3	–
$B_{\perp a}$	2.5	14.0	–

Table 2. Effective Landé factors g*.

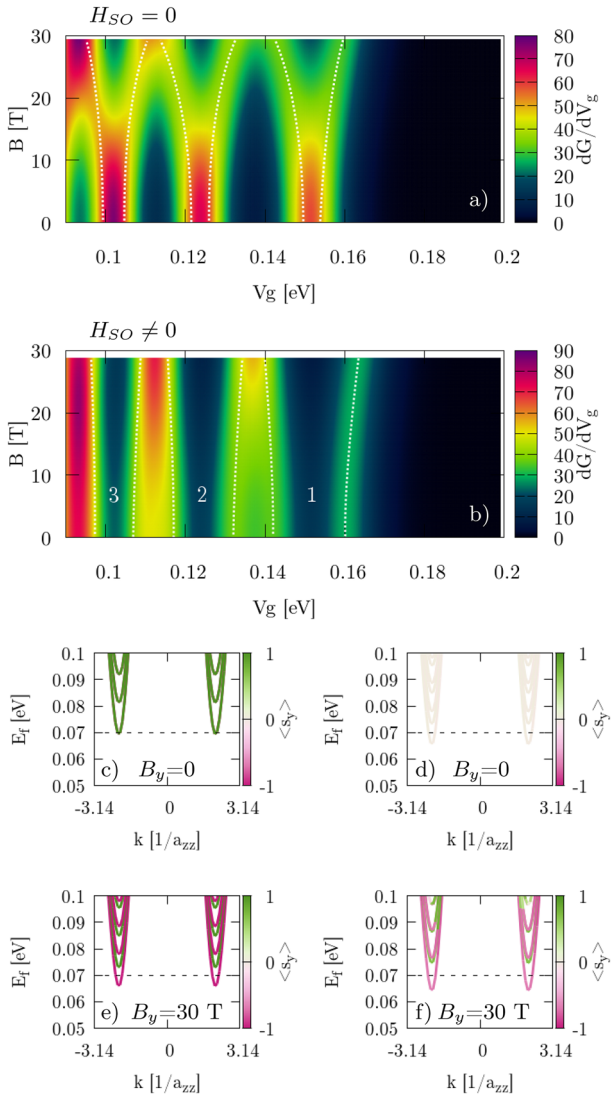

Figure 9. (**a**, **b**) Transconductance for the in-plane $\mathbf{B} = [0, B_y, 0]$ orientation of the magnetic field for zigzag edges. Double-spin states (of the same sign from both valleys) at E_F that enhance the conductance are marked by white dashed lines along the peaks. (**c**–**f**) Band structure for the center of the constriction. Colorbar indicates expected value of the spin projected to the y axis. Left column (**a**, **c**, **e**) corresponds to calculations with NO SOI part of the Hamiltonian, while right column (**b**, **d**, **f**) are with SOI part, respectively.

The second case concerns an in-plane magnetic field $B_\parallel$. We present the transconductance for the zigzag nanoribbon for $\mathbf{B} = [0, B_y, 0]$ (Fig. 9a, b) and we obtain similar results for $\mathbf{B} = [B_x, 0, 0]$ fields (not shown). For the armchair structure in $B_\parallel$ transconductance plots looks similar (not shown) and g^* were calculated separately.

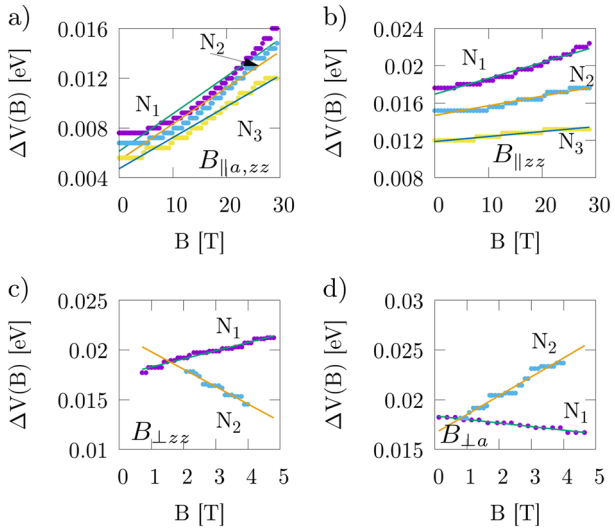

Figure 10. The splitting of the transconductance for parallel magnetic field $B_{\|}$ (**a**) without SO and (**b**) with SO term active. For perpendicular $B_{\perp}$ (**c**) in zigzag and (**d**) in armchair nanoribbon. The slope of the fitted line for each split in the transconductance (see Fig. 9a, b) is equal to $d(\Delta V_g(B))/dB$.

The new states that enhance the conductance at E_F come in pairs of the same spin-type for $B_y > 0$ (Fig. 9c–f). Again, the splitting at $B_y = 0$ is an effect of SO in KM form, but contrary to Fig. 7a this time we can calculate g^* from transconductance even if double-states are visible – the valley number in this case is not important. Slope of ΔV_g over B_y is calculated from the fit (Fig. 10) to the dashed lines in Fig. 9a, b. Results are presented in Table 2. Spin of an electron is strongly aligned along the z axis when SOI is taken into account, hence the impact of external in-plane magnetic field is suppressed and we observe decreased $g^* < 2$ values.

Summary and conclusions

We studied the effective g^* factors in electrostatic quantum point contacts defined in silicene using the tight-binding Hamiltonian by solving the scattering problem using the quantum transmitting boundary method. The spin–orbit coupling radically changes the values of the Landé factors. We showed that Zeeman splitting in magnetic field oriented parallel to the plane of the silicene lattice is isotropic and does not depend strongly on the edge type. Zeeman splitting from an external magnetic field is strongly suppressed by the intrinsic SO interaction in Kane–Mele form that introduces a Zeeman-like effective magnetic field perpendicular to the silicene plane. The spin–orbit interaction for the in-plane magnetic field decreases the effective g^* factor to $g_1^* = 1.2$ in the first subband, and $g_2^* = 0.78$, $g_3^* = 0.48$ for the next two in the zigzag structure, respectively. In armchair nanoribbon we obtain similar results for g^*: $g_1^* = 1.17$, moved slightly down/up/down $(-0.02, +0.14, -0.13)$ compared to zigzag for the 3 first subbands, due to the mirrored ν_{kj} sign that adds a local magnetic field energy in KM form.

For the perpendicular orientation of the magnetic field we obtain effective Landé factor $g_1^* = 5.8$ for the first subband and $g_2^* = 13.3$ for the second in a zigzag nanoribbon, and $g_1^* = 2.5$, $g_2^* = 14.0$ for the armchair edge type. Reasoning remains the same as in parallel case but now the interaction of SO coupling is more visible in the g^* factor for the first subbands, where local magnetic field significantly changes its value.

Received: 16 June 2021; Accepted: 17 September 2021
Published online: 06 October 2021

References

1. Thomas, K. J. *et al.* Possible spin polarization in a one-dimensional electron gas. *Phys. Rev. Lett.* **77**, 135 (1996).
2. Bhandari, N. *et al.* Steps toward an all-electric spin valve using side-gated quantum point contacts with lateral spin–orbit coupling. *Adv. Nat. Sci. Nanosci. Nanotechnol.* **4**, 013002 (2013).
3. Nowak, M. P. & Szafran, B. Spin current source based on a quantum point contact with local spin–orbit interaction. *Appl. Phys. Lett.* **103**, 202404 (2013).
4. Kim, S., Hashimoto, Y., Iye, Y. & Katsumoto, S. Evidence of spin-filtering in quantum constrictions with spin–orbit interaction. *J. Phys. Soc. Jpn.* **81**, 054706 (2012).
5. Aharony, A., Entin-Wohlman, O., Tokura, Y. & Katsumoto, S. Spin filtering by a periodic spintronic device. *Phys. Rev. B*https://doi.org/10.1103/physrevb.78.125328 *(2008).*
6. Eto, M., Hayashi, T. & Kurotani, Y. Spin polarization at semiconductor point contacts in absence of magnetic field. *J. Phys. Soc. Jpn.* **74**, 1934 (2005).
7. Meier, L. *et al.* Measurement of Rashba and Dresselhaus spin–orbit magnetic fields. *Nat. Phys.* **3**, 650 (2007).
8. Kane, C. L. & Mele, E. J. Quantum spin Hall effect in graphene. *Phys. Rev. Lett.* **95**, 226801 (2005).
9. Cummings, A. W., Garcia, J. H., Fabian, J. & Roche, S. Giant spin lifetime anisotropy in graphene induced by proximity effects. *Phys. Rev. Lett.* **119**, 206601 (2017).
10. Goulko, O., Bauer, F., Heyder, J. & von Delft, J. Effect of spin–orbit interactions on the 0.7 anomaly in quantum point contacts. *Phys. Rev. Lett.* **113**, 266402 (2014).

11. Pershin, Y. V., Nesteroff, J. A. & Privman, V. Effect of spin–orbit interaction and in-plane magnetic field on the conductance of a quasi-one-dimensional system. *Phys. Rev. B*https://doi.org/10.1103/physrevb.69.121306 *(2004).*
12. Scheid, M., Kohda, M., Kunihashi, Y., Richter, K. & Nitta, J. All-electrical detection of the relative strength of Rashba and Dresselhaus spin–orbit interaction in quantum wires. *Phys. Rev. Lett.*https://doi.org/10.1103/physrevlett.101.266401 *(2008).*
13. Martin, T. P. *et al.* Field-orientation dependence of the Zeeman spin splitting in (In, Ga) As quantum point contacts. *Phys. Rev. B* **81**, 041303 (2010).
14. Lu, F. *et al.* Enhanced anisotropic effective *g* factors of an $Al_{0.25}Ga_{0.75}N$/GaN heterostructure based quantum point contact. *Nano Lett.* **13**, 4654 (2013).
15. Qu, F. *et al.* Quantized conductance and large *g*-factor anisotropy in InSb quantum point contacts. *Nano Lett.* **16**, 7509. https://doi.org/10.1021/acs.nanolett.6b03297 (2016).
16. Li, L. *et al.* Quantum Hall effect in black phosphorus two-dimensional electron system. *Nat. Nanotechnol.* **11**, 593 (2016).
17. Zhou, X. *et al.* Effective *g* factor in black phosphorus thin films. *Phys. Rev. B* **95**, 045408 (2017).
18. Sichau, J. *et al.* Resonance microwave measurements of an intrinsic spin–orbit coupling gap in graphene: A possible indication of a topological state. *Phys. Rev. Lett.* **122**, 046403 (2019).
19. Lyon, T. J. *et al.* Probing electron spin resonance in monolayer graphene. *Phys. Rev. Lett.* **119**, 066802 (2017).
20. Mani, R. G., Hankinson, J., Berger, C. & de Heer, W. A. Observation of resistively detected hole spin resonance and zero-field pseudo-spin splitting in epitaxial graphene. *Nat. Commun.*https://doi.org/10.1038/ncomms1986 *(2012).*
21. Overweg, H. *et al.* Electrostatically induced quantum point contacts in bilayer graphene. *Nano Lett.* **18**, 553 (2017).
22. Overweg, H. *et al.* Topologically nontrivial valley states in bilayer graphene quantum point contacts. *Phys. Rev. Lett.* **121**, 257702 (2018).
23. Banszerus, L. *et al.* Observation of the spin–orbit gap in bilayer graphene by one-dimensional ballistic transport. *Phys. Rev. Lett.* **124**, 177701 (2020).
24. Lee, Y. *et al.* Tunable valley splitting due to topological orbital magnetic moment in bilayer graphene quantum point contacts. *Phys. Rev. Lett.* **124**, 126802 (2020).
25. Kraft, R. *et al.* Valley Subband splitting in bilayer graphene quantum point contacts. *Phys. Rev. Lett.* **121**, 257703 (2018).
26. Zhang, Y. *et al.* Direct observation of a widely tunable bandgap in bilayer graphene. *Nature* **459**, 820 (2009).
27. Oostinga, J. B., Heersche, H. B., Liu, X., Morpurgo, A. F. & Vandersypen, L. M. K. Gate-induced insulating state in bilayer graphene devices. *Nat. Mater.* **7**, 151 (2007).
28. Castro, E. V. *et al.* Biased bilayer graphene: Semiconductor with a gap tunable by the electric field effect. *Phys. Rev. Lett.* **99**, 216802 (2007).
29. Ohta, T., Bostwick, A., Seyller, T., Horn, K. & Rotenberg, E. Controlling the electronic structure of bilayer graphene. *Science* **313**, 951 (2006).
30. Mak, K. F., Lui, C. H., Shan, J. & Heinz, T. F. Observation of an electric-field-induced band gap in bilayer graphene by infrared spectroscopy. *Phys. Rev. Lett.* **102**, 256405 (2009).
31. Liu, C.-C., Feng, W. & Yao, Y. Quantum spin Hall effect in silicene and two-dimensional germanium. *Phys. Rev. Lett.* **107**, 076802 (2011).
32. Liu, M.-H. *et al.* Scalable tight-binding model for graphene. *Phys. Rev. Lett.* **114**, 036601 (2015).
33. Chowdhury, S. & Jana, D. A theoretical review on electronic, magnetic and optical properties of silicene. *Rep. Prog. Phys.* **79**, 126501 (2016).
34. Tao, L. *et al.* Silicene field-effect transistors operating at room temperature. *Nat. Nanotechnol.* **10**, 227 (2015).
35. Ezawa, M. Valley-polarized metals and quantum anomalous Hall effect in silicene. *Phys. Rev. Lett.* **109**, 055502 (2012).
36. Drummond, N. D., Zólyomi, V. & Fal'ko, V. I. Electrically tunable band gap in silicene. *Phys. Rev. B* **85**, 075423 (2012).
37. Tsai, W.-F. *et al.* Gated silicene as a tunable source of nearly 100% spin-polarized electrons. *Nat. Commun.* **4**, 1500. https://doi.org/10.1038/ncomms2525 (2013).
38. Shakouri, K., Simchi, H., Esmaeilzadeh, M., Mazidabadi, H. & Peeters, F. M. Tunable spin and charge transport in silicene nanoribbons. *Phys. Rev. B* **92**, 035413 (2015).
39. Ni, Z. *et al.* Tunable bandgap in silicene and germanene. *Nano Lett.* **12**, 113 (2011).
40. Danneau, R. *et al.* Zeeman splitting in ballistic hole quantum wires. *Phys. Rev. Lett.* **97**, 026403 (2006).
41. Martin, T. P. *et al.* Enhanced Zeeman splitting in $Ga_{0.25}In_{0.75}As$ quantum point contacts. *Appl. Phys. Lett.* **93**, 012105 (2008).
42. Kolasiński, K., Mreńca-Kolasinska, A. & Szafran, B. Transconductance and effective Landé factors for quantum point contacts: Spin–orbit coupling and interaction effects. *Phys. Rev. B* **93**, 035304 (2016).
43. Chen, M. X., Zhong, Z. & Weinert, M. Designing substrates for silicene and germanene: First-principles calculations. *Phys. Rev. B* **94**, 075409 (2016).
44. Fan, Y., Liu, X., Wang, J., Ai, H. & Zhao, M. Silicene and germanene on InSe substrates: Structures and tunable electronic properties. *Phys. Chem. Chem. Phys.* **20**, 11369 (2018).
45. Petrović, M. D. & Peeters, F. M. Fano resonances in the conductance of graphene nanoribbons with side gates. *Phys. Rev. B* **91**, 035444 (2015).
46. Liu, C.-C., Jiang, H. & Yao, Y. Low-energy effective Hamiltonian involving spin–orbit coupling in silicene and two-dimensional germanium and tin. *Phys. Rev. B* **84**, 195430 (2011).
47. Laubach, M., Reuther, J., Thomale, R. & Rachel, S. Rashba spin–orbit coupling in the Kane–Mele–Hubbard model. *Phys. Rev. B* **90**, 165136 (2014).

Acknowledgements

B.R. is supported by Polish government budget for science in 2017–2021 as a research project under the program "Diamentowy Grant" (Grant No. 0045/DIA/2017/46), by the EU Project POWR.03.02.00-00-I004/16 and NCN Grant UMO2019/32T/ST3/00044. A.M-K. is supported with "Diamentowy Grant" (Grant No. 0045/DIA/2017/46). The calculations were performed on PL-Grid Infrastructure on Prometheus at ACK-AGH Cyfronet.

Author contributions

The manuscript was written through the contributions of all authors. All the authors analyzed the data. All authors discussed the results and gave input on the manuscript. B.R. performed the calculations and wrote the paper.

Competing interests

The authors declare no competing interests.

Additional information

Correspondence and requests for materials should be addressed to B.R.

Reprints and permissions information is available at www.nature.com/reprints.

Publisher's note Springer Nature remains neutral with regard to jurisdictional claims in published maps and institutional affiliations.